Tailoring of crystal surface morphology by induced spatiotemporal oscillations of temperature

M. Khenner
Department of Mathematics, State University of New York at Buffalo, Buffalo, New York 14260, USA
(Received 17 April 2006; revised manuscript received 10 December 2006; published 23 February 2007)

This paper presents the model for pattern formation in the course of stable (unfaceted) and unstable (faceted) crystal growth from the vapor phase, which is influenced by the rapid spatiotemporal variations of the substrate and film temperature. In the model, such variations result from the interference heating of a substrate by weak pulsed laser beams. The ensuing form of the temperature field perturbation from the ground state is fairly generic and simple, and thus it may as well serve to model other situations. In the stable case the surface relaxational dynamics is influenced by surface diffusion transport of adatoms from the hot to the cold regions of a substrate; this leads to the accumulation of mass in the cold regions and depletion in the hot regions. In the unstable case the underlying faceting instability coupled to the directed diffusion transport leads to the formation of the stationary hill-and-valley structure, where the hills may terminate sharply or have the rough tops. The characteristic lateral scale of this structure increases as the wavelength of the temperature nonuniformity decreases, but the coarsening rate of the transients decreases. By effectively redistributing adatoms through the enhanced, spatially inhomogeneous diffusion the mechanism also delays the onset of the spatiotemporal chaos as the growth rate increases. These scenarios are modeled using the framework of the classical continuum theory of the morphological evolution, enriched with the recently developed regularization method for the ill-posed, unstable evolution partial differential equation (PDE), and coupled to the concept of the spatiotemporal oscillatory surface temperature as the "tailoring force" for the evolution dynamics. A mass-conserving finite volume method is developed that is capable of the accurate computation of the large-slope solutions of the unstable, strongly nonlinear, sixth order evolution PDE for the surface height.

DOI: 10.1103/PhysRevE.75.021605 PACS number(s): 81.15.Aa, 68.35.Fx, 68.55.Jk

I. INTRODUCTION

This paper presents a model for the morphological evolution of a surface of a continuous single-crystal film. As is well-known, such surfaces may undergo faceting (spinodal) instability when the film temperature is at, or below, the threshold temperature, T_f (temperature of the faceting transition). The faceting instability and subsequent coarsening of transient morphologies is the cause of formation of hill-and-valley structures on the thermodynamically unstable crystal surfaces [1,2]. Recently, a new approach was introduced by Zhang and Kalyanaraman [3–6] that allows the direct tailoring of the surface morphology during growth from vapor. In this approach, two pulsed laser beams are combined on the substrate for the interference heating. Thus the substrate is exposed to rapid spatiotemporal modulation. This method results in the film morphology that mimics the intensity distribution of the laser interference pattern. The experiments of Zhang and Kalyanaraman motivate this paper, where a model is developed for morphological evolution which is "driven" by induced temperature variations on the surface of the growing thin film. It must be noted here that the source and physical nature of a modulation may be different. For instance, not only weak laser pulses, but also oscillations of a potential in an electrochemical cell and high-amplitude surface ultrasound waves have been suggested as being capable of providing an alternative route for pattern formation on crystal surfaces [7]. In Ref. [7], the one-dimensional (1D) model for oscillatory-driven step motion on crystal surfaces is proposed. Also, Niu *et al.* [8] briefly considered implications of the modulation of the surface diffusion activation energy on epitaxial islands self-assembly. One important distinction between Refs. [7,8], where an abstract modulation is imposed, and this work is that this work is motivated by the experiments where the modulation has been achieved directly and its form and parameters are known with a high degree of precision. To put this paper in perspective, it must be mentioned here that thermodynamic and kinetic instabilities and coarsening of unstable surface structures have been (and are) intensively studied theoretically; see, for example, Refs. [9–18].

Since intensity and duration of irradiation are externally controlled parameters whose values may be broadly varied, we consider separately cases where the irradiation of a film with a pulsed, interfering laser beam (pulse duration $\sim$nanoseconds) results in the heating of a surface to a mean temperature which is too high ($T_0 > T_f$) or low enough ($T_0 \leqslant T_f$) for the faceting instability to occur. Following the experiment, it is assumed that in both cases the laser beam energy is insufficient to cause melting or degradation of a substrate and film; also, evaporation and recondensation are negligible. To help the reader understand the motivation, in Appendix B a short description of the experiments by Zhang and Kalyanaraman is provided.

When $T_0 > T_f$ the computations presented in Sec. III support the conjecture made by Zhang and Kalyanaraman about the nature of the new pattern formation scenario. It is demonstrated that the evolution of the initial surface morphology in the form of a preetched surface ripple leads to the formation of distinct surface features where the surface is colder, e.g., at the regions of the destructive interference. It must be emphasized that in this case there is no need for surface instabilities; the only requirement is externally controlled surface diffusion of adatoms from the (hot) regions of the

constructive interference to the (cold) regions of the destructive interference, and steady deposition in the direction normal to the surface.

When $T_0 \leqslant T_f$ the computations presented in Sec. IV demonstrate that this combination allows one to interfere in the process of the development of surface faceting instability, and to a certain extent tailor it so that a pattern with desired features and wavelength emerges. In studying the faceting instability and coarsening, a broad range of values of the parameter associated with the deposition from the vapor phase is considered. Another control parameter that is varied systematically is the separation distance of the adjacent interference fringes (equivalently, the wavelength of the surface temperature nonuniformity).

These scenarios are modeled using the framework of the classical continuum theory of morphological evolution of crystal surfaces, enriched with the recently developed regularization method for ill-posed, unstable evolution partial differential equations (PDEs). To be able to compute accurately the large-slope solutions of the unstable, strongly nonlinear, sixth order evolution PDE (with spatially dependent coefficients) for the surface height, a finite volume-type numerical method is developed. The method is tested on the results previously published by other authors.

High order parabolic PDEs describing surface-diffusion-driven morphological evolution of crystal surfaces become ill-posed and thus exhibit unstable solutions when a parameter describing anisotropy of the surface energy exceeds a certain threshold value [19]. The appearance of the threshold value is associated with the faceting transition [1,2]. To model the faceting instability, an ill-posed evolution equation must be regularized. The idea of regularization was first proposed by Herring [20] more than 50 years ago. Herring was concerned with the problem of determining the surface shape of a crystal in equilibrium. By considering constructions of the polar plots of the surface energy, he argued that it is necessary to include additional terms (proportional to powers of curvature) in the expressions for the surface energy. These terms penalize the sharp corners and make them rounded on a small length scale. Subsequently, Angenent and Gurtin [21] and Di Carlo *et al.* [22] derived a regularized PDE for the anisotropic motion-by-curvature (where the regularization term is proportional to the square of the curvature). Golovin *et al.* [23] extended these arguments as to the phenomenological proposition that the additional corner energy results from interaction of atomically high steps on a crystal surface in the vicinity of a corner. Regularization has been used for the description of equilibrium, as well as dynamical morphologies [23–27,29,30]. In Ref. [27], faceting by surface diffusion in the presence of the deposition from vapor was studied in detail using the long wavelength approximation. It was shown that the dynamics depends strongly on the growth rate parameter. For small values, hill-and-valley structure is formed that undergoes power-law coarsening. For larger values, stationary or oscillating structures are formed that do not undergo any coarsening. Further increase of the growth rate parameter leads to a chaotic spatiotemporal dynamics of the surface structures. Numerical methods for the computation with regularization have also been introduced [26,28,29]. A computational geometry tool which directly simulates coarsening of one million facets was very recently developed [30]. Finally, Stewart and Goldenfeld [1] and Watson and Norris [30] show a good match of models of thermal faceting based on unstable evolution PDEs to the experiments.

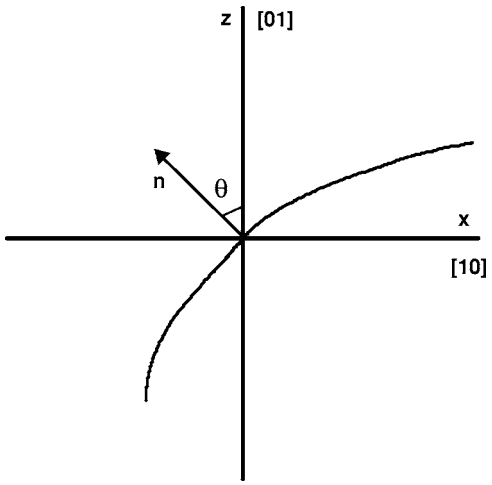

FIG. 1. Coordinate system.

II. MATHEMATICAL MODEL

Let a crystal grow due to a constant, unicomponent, normal flux of the material (typical to vapor-phase growth), which is adsorbed on the surface. Adsorbed atoms (adatoms) are redistributed by the surface diffusion. The surface is assumed clean and free of defects. Consider a model $1+1$ case corresponding to a two-dimensional crystal with a one-dimensional surface without overhangs but perhaps with large slopes. Thus the surface is described by a function $z=h(x,t)$.

Under these assumptions, the evolution of $h(x,t)$ is described by the following mass conservation PDE [31–33]:

$$\frac{h_t}{(1+h_x^2)^{1/2}} = V = F - \Omega j_s, \tag{1}$$

where V is the normal velocity of the curve representing the surface, F the vertical rate of a planar surface growth, Ω =const the atomic volume, j the surface diffusion flux, and s the arclength along the curve. In all equations in the paper the subscripts t, x, s, and θ denote differentiation.

The flux j is given by

$$j = -\frac{D\nu}{kT}\mu_s, \tag{2}$$

where D is the surface diffusivity, ν the (constant) surface density of adatoms, k the Boltzmann constant, T the absolute temperature, and μ the surface chemical potential.

The surface energy γ depends on orientation of the surface. The orientation is characterized by the angle θ that the local unit normal to the crystal surface makes with a particular crystalline direction, say [10] direction (Fig. 1). For a *fcc*-crystal, the anisotropy of the surface energy is usually given by the following fourfold symmetric form (see Ref. [34], for example):

$$\gamma(\theta) = \gamma_0(1 + \epsilon_\gamma \cos 4\theta), \tag{3}$$

where γ_0=const is the energy of forming a new vicinal surface of unit dimension and ϵ_γ=const>0 determines the degree of anisotropy. Above T_f Eq. (3) can be considered exact; below T_f it is approximate, and results from application of mathematical rounding to a discontinuity of $d\gamma(\theta)/d\theta$ at $\theta=0$, which is the orientation of a facet [34]. At and below T_f the anisotropy of γ is strong ($\epsilon_\gamma > 1/15$), and the stiffness

$$G(\theta) = \gamma + \gamma_{\theta\theta} = \gamma_0(1 - 15\epsilon_\gamma \cos 4\theta) \tag{4}$$

is negative in certain intervals of values of θ. This manifests in the appearance of corners on the equilibrium Wulff shape of a crystal [20]; in the dynamical case, the evolution equations become backward-parabolic and unstable where $G<0$, see, for example, Refs. [22,23,26,35]. As mentioned in Ref. [22], "the angle intervals in which stiffness is negative are very much like the spinodals encountered in the Cahn-Hilliard theory of phase transitions" [36]. To track surface evolution with the strongly anisotropic surface energy, the problem must be regularized in order to penalize the instability. Thus the expression for the surface energy becomes [2,22]

$$\gamma(\theta, \kappa) = \gamma_0(1 + \epsilon_\gamma \cos 4\theta) + \frac{\delta}{2}\kappa^2, \tag{5}$$

where δ=const>0 is the small regularization parameter having units of energy, and

$$\kappa = \theta_s = \frac{-h_{xx}}{(1 + h_x^2)^{3/2}} \tag{6}$$

is the local curvature. The factor of 2 in the regularization term is purely for convenience.

The chemical potential in the presence of the regularization has the form [23]

$$\mu = \Omega[G(\theta) - H]\kappa, \quad H = \kappa\left(\frac{1}{2} + \frac{d^2}{d\theta^2}\right)\left(\frac{\partial\gamma}{\partial\kappa}\right) + \frac{\partial^2\gamma}{\partial\kappa^2}\left(\frac{d\kappa}{d\theta}\right)^2. \tag{7}$$

Equations (4)–(7) yield the compact form of the regularized chemical potential:

$$\mu = \Omega\gamma_0\left[1 - 15\epsilon_\gamma \cos 4\theta - \frac{\delta}{\gamma_0}\left(\frac{1}{2}\kappa^2 + \frac{\kappa_{ss}}{\kappa}\right)\right]\kappa \equiv \Omega\gamma_0 W(\theta, \theta_s)\kappa. \tag{8}$$

It is easy to see that the evolution equation (1) is fourth-order when the anisotropy is weak and the regularization is not needed (δ=0) and sixth-order when the anisotropy is strong and the equation is regularized.

The three parameters of a continuum model that generally depend on temperature are the diffusivity D, the mean surface energy γ_0, and the degree of anisotropy ϵ_γ.

The dependence of the surface diffusivity on temperature is described by the Arrhenius expression

$$D(T) = D_0 \exp\left(\frac{-E_d}{kT}\right), \tag{9}$$

where D_0=const is the prefactor and E_d=const is the activation energy. The temperature dependence of the mean surface energy is usually a linear function

$$\gamma_0 = \gamma_{00} - ST, \tag{10}$$

where γ_{00} is the energy at $T=0$ and S is the entropy per atom of the surface. Thus the mean surface energy decreases with increasing temperature. Next, for temperatures below the temperature of faceting transition T_f, the form $\epsilon_\gamma(T)$ is given by the theory of second-order phase transitions [37]:

$$\epsilon_\gamma = \epsilon_0 \exp\left(\frac{-E_0}{(T_f - T)^{1/2}}\right), \tag{11}$$

where ϵ_0 and E_0 are constant parameters. For temperatures above T_f the anisotropy coefficient ϵ_γ decreases approximately linearly with T. In the first approximation, the linear interpolation between the two domains (in the vicinity of the critical value $\epsilon_\gamma = 1/15$) gives

$$\epsilon_\gamma = \zeta(T_f - T) + 1/15, \quad \zeta > 0. \tag{12}$$

Since $\epsilon_\gamma \geqslant 0$, Eq. (12) imposes a restriction on the maximum temperature in the model: $T_{\max} \leqslant T_f + 1/(15\zeta)$. This inequality, in fact, gives an upper bound on the output power intensity of the laser source (weak heating of the target). This is consistent with the proposed modeling framework and the experiment. Accounting for the dependence (12) (or for a more accurate one) simultaneously with spatially nonuniform heating [see Eq. (17) below, which implies $T_{\max} = T_0(1 + |\hat{T}(x,t)|)$] results in a model where the surface energy anisotropy depends not only on the crystallographic orientation of the surface, but also on the position along the substrate, as some regions are hotter than others. Note that accounting for the temperature dependence of γ_0 via Eq. (10) rescales the coefficients of the resulting PDE but does not change its form. Also, Eq. (12) introduces one additional parameter. In this paper a minimal model is built that does not account for the surface energy anisotropy dependence on temperature via Eq. (12). Instead, the faceting transition is factored in simply by increasing the parameter ϵ_γ from below to the critical value 1/15. The critical value, in turn, occurs when the mean substrate (and film) temperature T_0 approximately equals the temperature of the faceting transition T_f. Thus the explicit temperature dependence enters in the minimal model only through the surface diffusivity D.

Substitution of Eqs. (2), (8), and (9) into Eq. (1) [and noting that $\partial/\partial s = (1 + h_x^2)^{-1/2}\partial/\partial x$] yields the following surface evolution equation:

$$h_t = F\sqrt{1 + h_x^2} + A\frac{\partial}{\partial x}\left(\frac{\exp(-E_d/kT)}{kT}(1 + h_x^2)^{-1/2}\frac{\partial}{\partial x}\kappa W(\theta, \theta_s)\right), \tag{13}$$

where $A = \Omega^2 \nu D_0 \gamma_0$.

Equation (13) admits the trivial solution

$$h = h(t) = Ft + h_0, \quad h_0 = \text{const} \tag{14}$$

at any temperature $T=T(x,t)$. This solution corresponds to a crystal with planar surface growing vertically at constant rate F. Without loss of generality the reference value h_0 can be chosen as zero. Assume now that the entire surface of the horizontal dimension L is irradiated by laser pulses.

Far from the melting threshold, pulsed laser irradiation gives rise to a quasistationary state in which the temperature of the irradiated section of a surface fluctuates about the mean value T_0 with a frequency ω of the source pulse repetition. For instance, in the experiments [38] and simulations [39,40] using metallic films, the quasistationary state is achieved after as few as 4 to 5 laser pulses. Consider perturbation $h=\tilde{h}(x,t)$ of the steady state (14), and simultaneous perturbation of the mean temperature field, $T=T_0+\tilde{T}(x,t)$, such that $|\tilde{T}(x,t)/T_0| \equiv |\hat{T}(x,t)| \ll 1$. Next, the tilde sign over h is omitted and the transformation is made to the frame of reference moving in the z direction with the speed F (via changing h to $h-Ft$).

Finally, $\exp\left(\frac{-E_d}{kT}\right)/(kT)$ in Eq. (13) is expanded in powers of $\hat{T}(x,t)$:

$$h_t = F(-1+\sqrt{1+h_x^2}) + A\frac{\partial}{\partial x}\Bigg[(a_0 + a_1\hat{T} + a_2\hat{T}^2)(1 + h_x^2)^{-1/2}\frac{\partial}{\partial x}\kappa W(\theta,\theta_s)\Bigg], \tag{15}$$

where the coefficients

$$a_0 = \frac{\exp\left(\frac{-E_d}{kT_0}\right)}{kT_0}, \quad a_1 = a_0\left(\frac{E_d}{kT_0} - 1\right), \quad a_2 = a_0\left[\frac{1}{2}\left(\frac{E_d}{kT_0}\right)^2 - 2\frac{E_d}{kT_0} + 1\right] \tag{16}$$

have dimension of the inverse energy. It has been shown in [41] by the direct numerical comparison with higher-order expansions that expansion up to second order allows one to predict surface shapes (in the course of morphological relaxation) with sufficient accuracy.

To close the model, the realistic form for the temperature perturbation $\hat{T}(x,t)$ is required. The following form is used:

$$\hat{T}(x,t) = (Q_0 \cos \omega t)(1 + Q_1 \cos qx). \tag{17}$$

This form approximates well [6] the one-dimensional interference fringes (on a planar horizontal surface) from the two pulsed beams, which originate from a split single, pulsed laser beam. $0<Q_0 \ll 1$ determines the magnitude of small temporal oscillations about T_0 due to the pulsed nature of irradiation. On the other hand, $0<Q_1<1$ determines the difference of mean temperatures at the regions (fringes) of the constructive and destructive interference. Distance d between the centers of two adjacent fringes is related to the angle that two beams form. If this angle is 2ϕ, then $d=2\pi/q = \ell/(2\sin\phi)$, where ℓ is the wavelength of a laser pulse [3]. Parameters Q_0, Q_1, and the mean temperature T_0 are known functions of the power density of the radiation, the absorptivity of the surface at the radiation wavelength, and the thermophysical and optical characteristics of the material [38,39]. It must be noted that the simple form (17) ignores effects of the height variation of the film surface on the interference picture; these effects were considered in Ref. [41] for the case of pure relaxational, isotropic evolution dynamics without deposition. As a rule, they are small if the height variation is small; this is so in our model and in the experiments (see Appendix B).

Zhang and Kalyanaraman used a pulsed ultraviolet laser with the pulse width 9 ns and the repetition frequency 50 Hz [3]. They note that for most metals on Si, the diffusion distance in a 9 ns time scale is of the order of 2 nm under isothermal conditions, and thermal gradients are likely to increase this distance. The deposition time needed to form 3.2 nm tall structures was 10 min. This time encompasses 30 000 pulses. Thus to model the surface evolution on the long time scale associated with the formation of structures at least a few nanometers high, it is sufficient to use Eq. (15) where the coefficients that involve the temperature perturbation are averaged over the period of pulse repetition, $2\pi/\omega$. In other words, the differentiation on the left-hand side of Eq. (15) is treated as being with respect to "slow" time associated with the typical long time scale of morphological changes due to surface diffusion, while the form (17) involves "fast" time associated with the short duration of a laser pulse. Averaging is with respect to fast time, during which the film height is constant.

In the next section the small slope approximation is derived and the computations with this approximation are described. The numerical method for the computation with (nondimensionalized and averaged) Eq. (15) and the results are presented in Sec. IV.

III. SMALL SLOPE APPROXIMATION ($|h_x| \ll 1$)

To derive the PDE in this frequently used approximation, we note that $\cos 4\theta = 8(\cos^4\theta - \cos^2\theta) + 1$, where $\cos\theta = (1+h_x^2)^{-1/2}$ (see Fig. 1) and substitute Eqs. (6), (8), and (17), and $\cos 4\theta$ into Eq. (15). Then, Eq. (15) is expanded in powers of h_x up to second order and averaged.

The result is the sixth order ($\partial/\partial x \sim \epsilon \ll 1$) nondimensional PDE:

$$h_t = \frac{1}{2}fh_x^2 + B(1+\alpha\langle\hat{T}^2\rangle)(\Lambda_1 h_{xxxx} - 3\Lambda_1 h_{xx}^3 + \Lambda_2 h_x h_{xx} h_{xxx} + \Lambda_3 h_{xxxx} h_x^2) + B\alpha\langle\hat{T}\hat{T}_x\rangle(2\Lambda_1 h_{xxx} + 2\Lambda_3 h_{xxx} h_x^2 + \Lambda_4 h_{xx}^2 h_x) + B\Delta(2\alpha\langle\hat{T}\hat{T}_x\rangle h_{xxxxx} + (1+\alpha\langle\hat{T}^2\rangle)h_{xxxxxx}), \tag{18}$$

where $f=F/(L\omega)$, $B=a_0A/(\omega L^4)$, $\bar{q}=qL$, $\Delta=\delta/(\gamma_0 L^2)$, and $\alpha=a_2/a_0$. These parameters are positive. Also,

$$\Lambda_1 = 15\epsilon_\gamma - 1, \quad \Lambda_2 = 10(1-63\epsilon_\gamma), \tag{19}$$

$$\Lambda_3 = 2(1-75\epsilon_\gamma), \quad \Lambda_4 = 6(1+65\epsilon_\gamma); \tag{20}$$

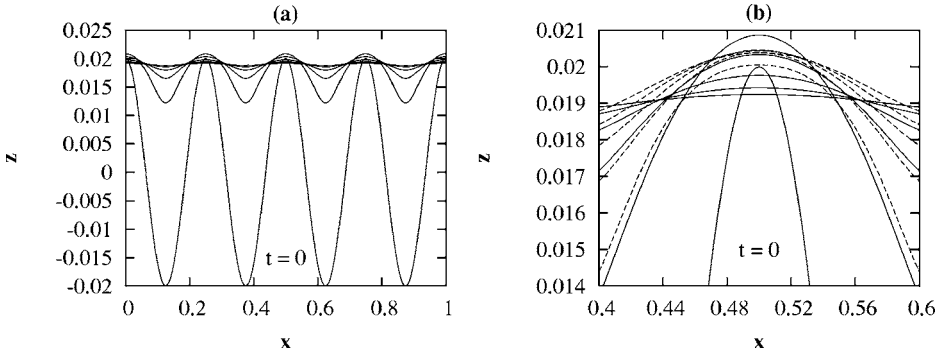

FIG. 2. Relaxation of the small-slope, 1D surface perturbation in the case of isotropic surface energy ($\epsilon_\gamma=0$) and equal wavelengths of the temperature perturbation and the surface perturbation ($\lambda_T=\lambda_S$). $f=10^{-6}$. (a) Full view. (b) Zoom in the center and the comparison to the profiles obtained in the isothermal case ($Q_0=0$; dashed lines).

$$\langle \hat{T}^2 \rangle = \frac{1}{2} Q_0^2 (1 + Q_1 \cos \bar{q}x)^2 > 0, \quad \langle \hat{T}\hat{T}_x \rangle = -\frac{1}{2} Q_0^2 Q_1 \bar{q} \left(\sin \bar{q}x + \frac{1}{2} Q_1 \sin 2\bar{q}x \right). \tag{21}$$

$1/\omega$ has been used for unit of time and L for unit of length. The 2π-based scale for the nondimensional wave number is convenient, thus changing in Eq. (21) $\bar{q}$ to $2\pi\bar{q}$ yields

$$\langle \hat{T}^2 \rangle = \frac{1}{2} Q_0^2 (1 + Q_1 \cos 2\pi\bar{q}x)^2 > 0, \quad \langle \hat{T}\hat{T}_x \rangle = -\pi Q_0^2 Q_1 \bar{q} \left(\sin 2\pi\bar{q}x + \frac{1}{2} Q_1 \sin 4\pi\bar{q}x \right). \tag{22}$$

The first term on the right-hand side of Eq. (18) is the typical Kardar-Parisi-Zhang (KPZ)-type nonlinearity caused by the normal growth [42]; the second, linear term ($\sim \Lambda_1 h_{xxxx}$) describes relaxation of an arbitrary perturbation if the surface energy anisotropy is weak ($\epsilon_\gamma \leqslant 1/15$), and amplification (faceting instability) otherwise. The very last linear term ($\sim \Delta h_{xxxxxx}$) ensures stability with respect to short wavelength perturbations, and the three nonlinear terms in the first line of the equation are responsible for ultimate stabilization of the surface slope and vanishing of the growth rate of a perturbation [23,26–28,35]. All third and fifth order terms are retained, since unlike the isothermal case [27] their presence does not break the invariance with respect to transformation $x \leftrightarrow -x$ (due to the presence of the multiplier $\langle \hat{T}\hat{T}_x \rangle$ which changes sign at the transformation); such invariance reflects the fourfold symmetry of the crystal surface.

Remarks.

(1) When the conditions are isothermal ($Q_0=0$), Eq. (18) reduces, after appropriate rescaling, to the convective, sixth-order Cahn-Hilliard equation studied in Ref. [27].

(2) When the conditions are isothermal and the deposition is absent ($f=0$), Eq. (18) takes the form (after linearization) [26]:

$$h_t = B(\Lambda_1 h_{xxxx} + \Delta h_{xxxxxx}). \tag{23}$$

The second, regularization term must be kept in Eq. (23) if the surface energy anisotropy is strong ($\Lambda_1 > 0$). Otherwise, it has to be omitted. Equation (23) has plane wave solutions $h_k(x,t)$ given by

$$h_k = C \exp(\omega(k)t) \cos kx, \quad \omega(k) = \Lambda_1 k^4 - \Delta k^6. \tag{24}$$

Unstable modes k obeying $\omega(k) > 0$ are given by $k < \sqrt{\Lambda_1/\Delta}$. The maximum growth rate

$$\omega_{\max} = \frac{16\pi^4 \Lambda_1}{3\lambda_{\max}^4} \tag{25}$$

is achieved for the wavelength

$$\lambda_{\max} = 2\pi\sqrt{3\Delta/2\Lambda_1}. \tag{26}$$

Thus the most unstable wavelength is determined by the balance between the corner regularization energies and the surface energy anisotropy causing the spinodal decomposition of the planar surface. $\lambda_{\max}$ will be referred to as the "spinodal" wavelength.

In the next two sections, the focus is on the nonisothermal situation ($Q_0 \neq 0$) with the isotropic (Sec. III A) or strongly anisotropic (Sec. III B) surface energy. As has been noted above, in the former case $T_0 > T_f$ and the faceting instability

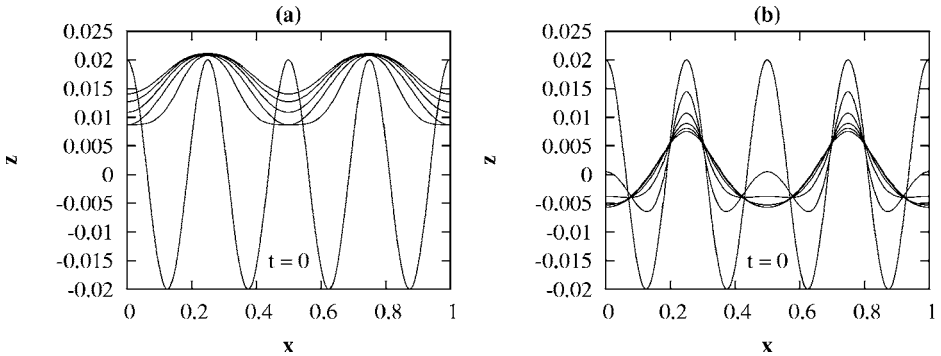

FIG. 3. Relaxation of the small-slope, 1D surface perturbation. $\epsilon_\gamma=0$, $\lambda_T=2\lambda_S$. (a) $f=10^{-6}$. (b) $f=10^{-9}$.

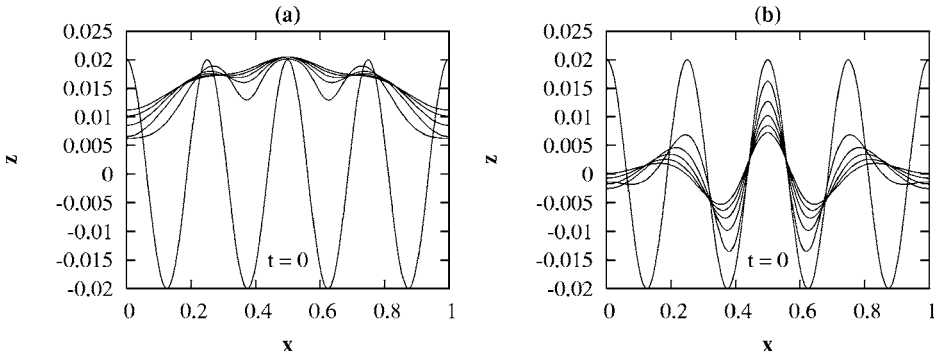

FIG. 4. Same as Fig. 3, but $\lambda_T=4\lambda_S$.

is absent. This case is reminiscent of the experiments by Zhang and Kalyanaraman.

A. Case of surface energy γ isotropic ($\epsilon_\gamma=0$)

In the absence of anisotropy the regularization is not needed. Thus Δ is set to zero in Eq. (18). This eliminates the fifth- and sixth-order linear terms from the equation. Also, the fifth- and sixth-order nonlinear terms must not be kept in the equation when there is no corresponding linear terms, and therefore such terms are omitted. Then the PDE takes the simpler form:

$$h_t = \frac{1}{2} f h_x^2 - B[(1 + \alpha\langle\hat{T}^2\rangle)h_{xxxx} + 2\alpha\langle\hat{T}\hat{T}_x\rangle h_{xxx}], \quad (27)$$

where $\langle\hat{T}\rangle$ and $\langle\hat{T}\hat{T}_x\rangle$ are given by Eqs. (22). Equation (27) is fourth-order. Notice that under the isothermal conditions (without the deposition) Eq. (27) further reduces to the classical, linear Mullins equation $h_t=-Bh_{xxxx}$ [31]. The surface diffusion part of Eq. (27) does not contain nonlinear terms but the coefficients are functions of the space coordinate x. It is demonstrated next that this results in unusual dynamics. The unusual form of Eq. (27) [see also Eq. (28) below] has parallels in models for liquid films. For instance, Pototsky *et al.* [43] and Haskett *et al.* [44] recently proposed models where the PDEs with spatially varying coefficients are formulated to describe thin liquid films driven by external disturbances.

Equation (27) was solved using the method of lines procedure, which involves uniformly fourth-order accurate finite difference discretization in space and implicit Runge-Kutta integration in time. Periodic boundary conditions were used. The initial condition is the cosine curve $h(x,0)=0.02\cos 8\pi x$. The wavelength of this perturbation is denoted λ_S (=1/4). Since reliable material parameter values for the Co-Si system are difficult to find, for the purpose of concept proof the well-established values for the GaAs-GaAs system are used in this paper; the parameter values are listed in Ref. [41]. Then, $B=5\times10^{-13}$, $\alpha=43$. We take $Q_0=0.5$, $Q_1=0.99$ and $f=10^{-6}$ or 10^{-9} (for comparison, the value of f calculated using data in Ref. [3] is 3×10^{-8}; this is based on $F=0.1$ nm/min, $\omega=50$ Hz, and $L=10\times d=10$ μm). The parameter $\bar{q}$ was varied. Computations were done with the grid spacing $\delta x=0.01$ and, for $\bar{q}\geqslant 10$, also with $\delta x=0.005$. In Figs. 2(a) and 3–5, the profile that has the smallest value at the boundaries of the computational domain is the last computed profile [in Fig. 2(b) the last computed profile appears to have the largest value at the zoom window frame]. In Appendix A the results of a few simulations using the isotropic, 2+1, large-slope model are presented.

(1) Computations with $\lambda_T\geqslant\lambda_S$. Figure 2 shows the relaxation of the initial profile for the case $\bar{q}=4$. Thus the wavelength of the temperature perturbation, $\lambda_T=1/\bar{q}$, equals that of the surface perturbation λ_S. Notice that λ_T has the meaning of the nondimensional distance between the centers of the adjacent interference fringes, $\bar{d}$ [see the discussion after Eq. (17)]. The transient shapes of the surface are very different from the initial cosine curve [Fig. 2(a)] since the minima relax much faster than maxima. Interestingly, at an early stage the surface overshoots the initial maximum value. Also note that the surface relaxes to the nonzero level $z<\approx 0.02$. (At first glance, this should not be expected since computations are done in the moving reference frame. However, as stated above, the reference frame moves in the z direction with the speed (=F) of planar surface growth; but, the nonplanar surface, having larger arclength, grows faster [Eq. (1) states that in the absence of surface diffusion the rate of

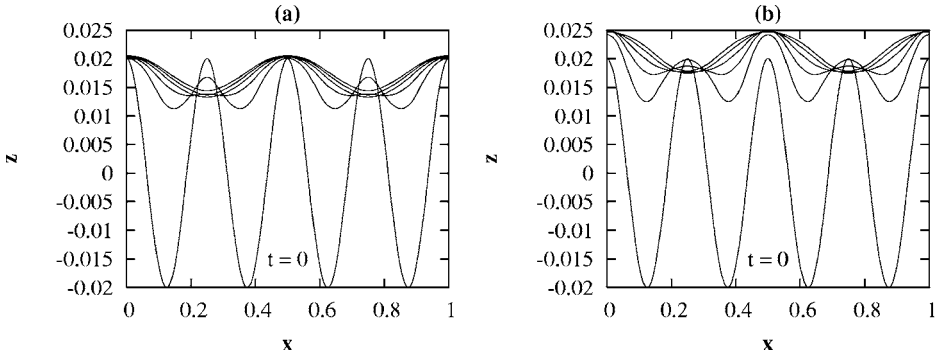

FIG. 5. Relaxation of the small-slope, 1D surface perturbation. $\epsilon_\gamma=0$, $f=10^{-6}$. (a) $\lambda_T=(2/3)\lambda_S$. (b) $\lambda_T=0.4\lambda_S$.

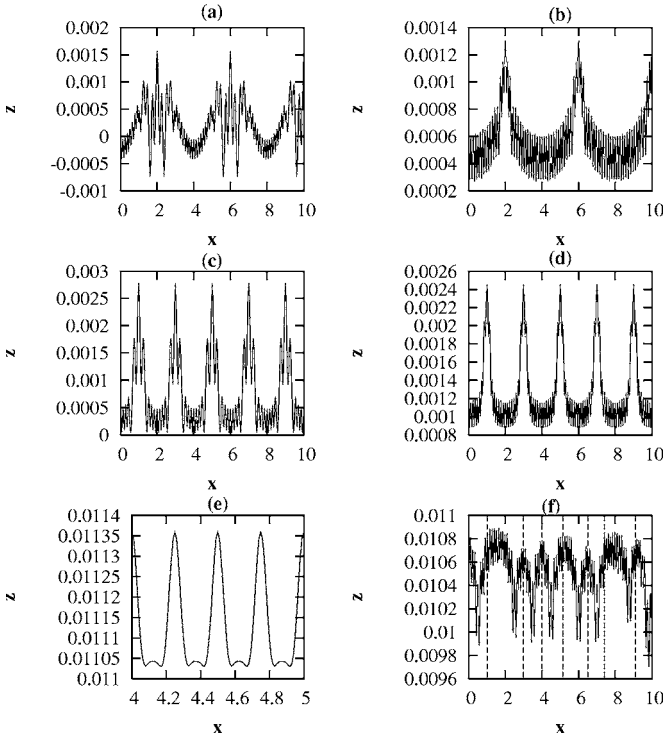

FIG. 6. Surfaces (b), (d), and (f) are stationary. Results of the numerical integration of Eq. (18) with strong surface energy anisotropy. $\epsilon_\gamma=0.066\,733$. $\bar{q}=0.25$ [(a) and (b)], 0.5 [(c) and (d)], and 4 [(e) and (f)]. Surface is captured at $t=10^9$ [(a), (c), and (e)] and $t=2\times10^{10}$ [(b), (d), and (f)]. In (e), the surface has to be periodically extended to the left and to the right for the full view. The high-frequency wavy structure between the high-amplitude peaks in (a)–(d) is *not* the numerical instability; it is the physical faceted structure with the uniform wavelength $\lambda\approx0.1\pm0.01$, where 0.1 is value of the spinodal wavelength $\lambda_{\max}$. The fine structure of these regions (not shown) can be imagined from the shape in (e) by extending the minor peaks at the bottom to the height of major peaks.

change of film height is $F(1+h_x^2)^{1/2}$]. This nonconformity manifests as mass gain in Fig. 2. Of course, the mass gain would be even larger were the computations performed in the laboratory frame.) Figure 2(b) shows that the temperature nonuniformity influences significantly the profile evolution even in this case of equal wavelengths.

Next, Fig. 3 shows the relaxation of the same initial profile for the case $\bar{q}=2$ (thus the temperature maximum occurs at the first, third, and fifth (last) maxima of the surface, and the temperature minimum occurs at the second and the fourth maxima of the surface). One can see *coarsening* of the perturbation—the material accumulates in the vicinity of $x=0.25$ and 0.75 due to diffusive transport from the adjacent hotter regions in the vicinity of $x=0$, 0.5, and 1. This is exactly the mechanism Zhang and Kalyanaraman proposed as part of the explanation of their experimental data, but have not been able to prove. The accumulation of the material at colder regions results in slowly decaying surface spikes.

For completeness, Fig. 4 shows the case $\bar{q}=1$ ($\lambda_T=4\lambda_S$). Note that at strong nonlinearity the transient surface profiles are very smooth.

(2) Computations with $\lambda_T<\lambda_S$. In this case either the coarsening is absent or it occurs but the details are only weakly sensitive to the wavelength λ_T. Coarsening is absent when the wavelength of the temperature perturbation is related to the wavelength of the surface perturbation as $\lambda_T=\lambda_S/2^i$, $i=1,2,\ldots$, and/or $\lambda_T\leqslant1/12$. In these cases the profile evolution is similar, at large, to the isothermal evolution (note that rates of decay and extrema widths differ from the isothermal one). Figure 5 shows the evolution for $\bar{q}=6$ and 10, with $f=10^{-6}$. One can see that the second and fourth maxima become extinct from the shape. Overall, at large times these shapes are similar to the one shown in Fig. 3(a), except that they are out of phase with that shape.

B. Case of surface energy γ strongly anisotropic

We now take $\epsilon_\gamma=0.066\,733$, $\Delta=1.72\times10^{-7}$ and compute with Eq. (18). The spinodal wavelength and growth rate corresponding to these values are $\lambda_{\max}=0.1$ and $\omega_{\max}=5000$, respectively. The initial condition is the same, $h(x,0)=0.02\cos8\pi x$, but on the longer domain $0\leqslant x\leqslant10$ and $f=10^{-9}$. Periodic boundary conditions were used in computations, except for $\bar{q}=0.25$ (in which case the ratio of the domain size to λ_T is not an integer). In this case the symmetry boundary conditions $h_x=h_{xxx}=0$ were used. Computations were done with $\delta x=0.01$ and 0.005. The results for the two grid resolutions coincide.

Figure 6 shows the snapshots of the surface for $\bar{q}=0.25$, 0.5, and 4, each at two values of t (small and large). The large t-value surfaces are stationary (do not undergo further coarsening). The initial surface undergoes deformation under the combined action of KPZ-nonlinearity, faceting instability and diffusive mass transfers from hotter to colder regions. In Figs. 6(a)–6(d) this results in the formation of the stationary sharply peaked structures exactly where the surface is the most cold. Notice that in Fig. 6(f), where $\lambda_T/\lambda_S=1/4:1/4$

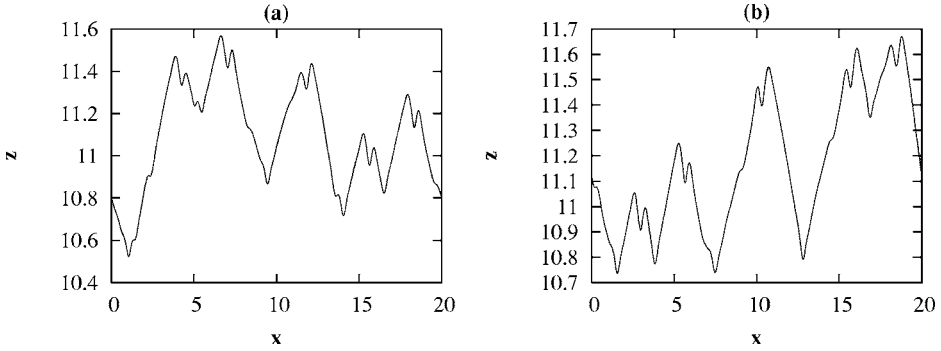

FIG. 7. Stationary ($t=2\times10^9$) results of the numerical integration of Eq. (28) with strong surface energy anisotropy. $\epsilon_\gamma=0.5$, $\bar{q}=1.5$, and $f=10^{-7}$. (a) Grid resolution $\delta x=0.02$. (b) $\delta x=0.01$.

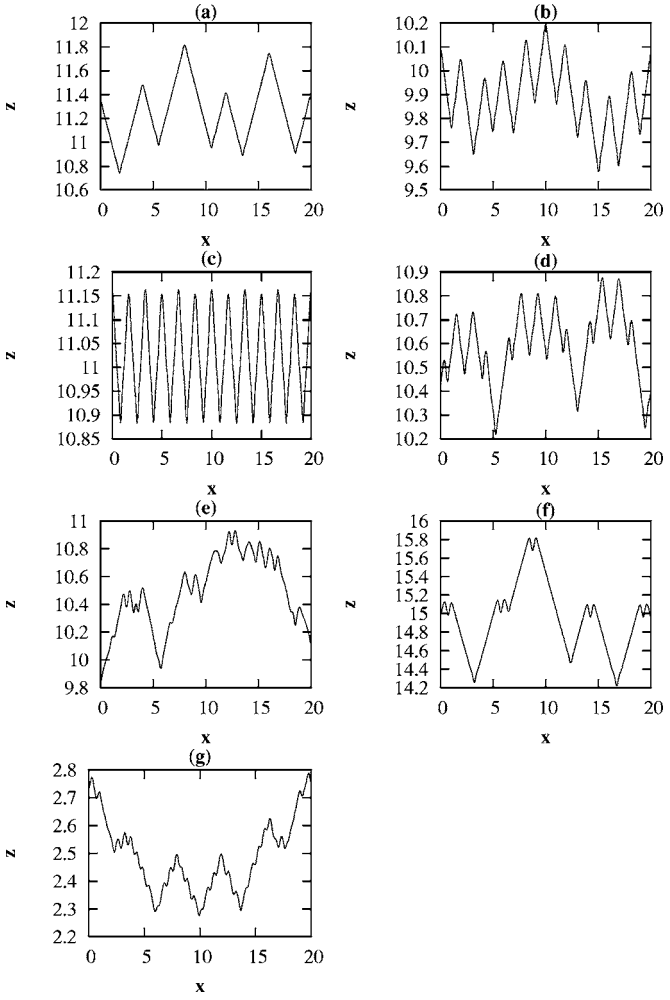

FIG. 8. Stationary ($t=2\times10^9$) surface shapes resulting from the numerical integration of Eq. (28). $\epsilon_\gamma=0.5$, $f=10^{-7}$. $\bar{q}$=(a), 0.25, (b) 0.5, (c) 0.6, (d) 0.65, (e) 1, (f) 2, and (g) 0.25. The last shape has been obtained using the standard finite difference method and is shown for comparison with (a).

$=1$ the structure wavelength is not constant and the number of wavelengths (8) is much less than expected (40). We find similar behavior in the fully nonlinear problem (for large $\bar{q}$); see next section.

On the bad side, the numerical integration fails for $\bar{q}=2$ and 8 even when a very fine spatial grid is used. This motivated us to develop a more elaborate numerical method for the integration of the fully nonlinear evolution PDE. The method is described in the next section. Compared to the standard method, this method has superior mass-conservation and convergence properties and it is, on average, three to six times faster. In the fully nonlinear simulations the acceleration is achieved due to effective numerical averaging of the small-scale oscillations (spinodals).

IV. FULLY NONLINEAR MODELING

Equation (15) takes the following form after the nondimensionalization and averaging:

$$h_t = f(-1+\sqrt{1+h_x^2}) + B\frac{\partial}{\partial x}\left[(1+\alpha\langle\hat{T}^2\rangle)(1+h_x^2)^{-1/2}\frac{\partial}{\partial x}\kappa W(\theta,\theta_s)\right]. \tag{28}$$

Nondimensional parameters are the same as for Eq. (18), the averaged square of the temperature perturbation is given by the first of Eqs. (22), and $W(\theta,\theta_s)$ has been defined in Eq. (8).

A. Nested finite volume method

Equation (28) is discretized as follows, given $x_i=i(\delta x)$, $i=0\cdots N$, $\delta x=x_N/N$:

$$\frac{dh_i}{dt} = fP_i + B\frac{(1+\alpha R_{i+1/2})S_{i+1/2}-(1+\alpha R_{i-1/2})S_{i-1/2}}{\delta x}, \tag{29}$$

where

$$P_i = \frac{1}{2}\{[1+h_x(i+1/2)^2]^{1/2}+[1+h_x(i-1/2)^2]^{1/2}-2\}, \tag{30}$$

$$R_{i\pm1/2} = \frac{1}{2}Q_0^2\left[1+Q_1\cos\left(2\pi\bar{q}\left(x_i\pm\frac{\delta x}{2}\right)\right)\right]^2, \tag{31}$$

$$S_{i\pm1/2} = U_i^{(\pm1/2)} - \Delta V_i^{(\pm1/2)}. \tag{32}$$

It is shown next how to compute P_i and $S_{i\pm1/2}$.

Derivatives h_x and h_{xx} are approximated at the center of the interval $[i,i+1]$ as

$$h_x(i+1/2) = \frac{1}{2}[h_x(i)+h_x(i+1)], \tag{33}$$

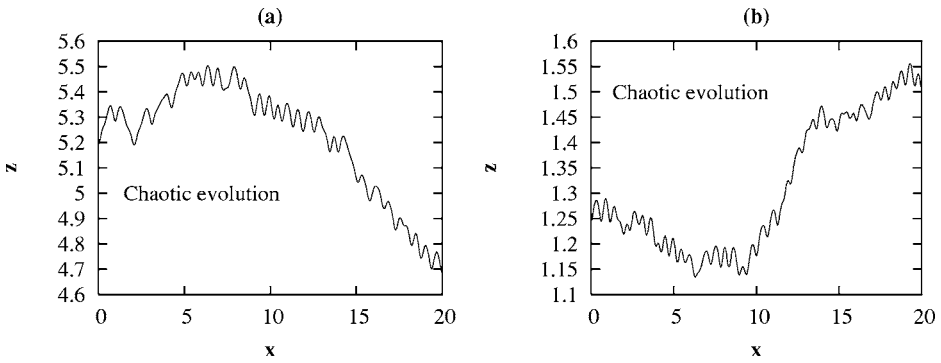

FIG. 9. Snapshot of the surface at $t=2\times10^9$. (a) Nonisothermal case, $\bar{q}=8$. (b) Isothermal case ($Q_0=0$). $\epsilon_\gamma=0.5$, $f=10^{-7}$.

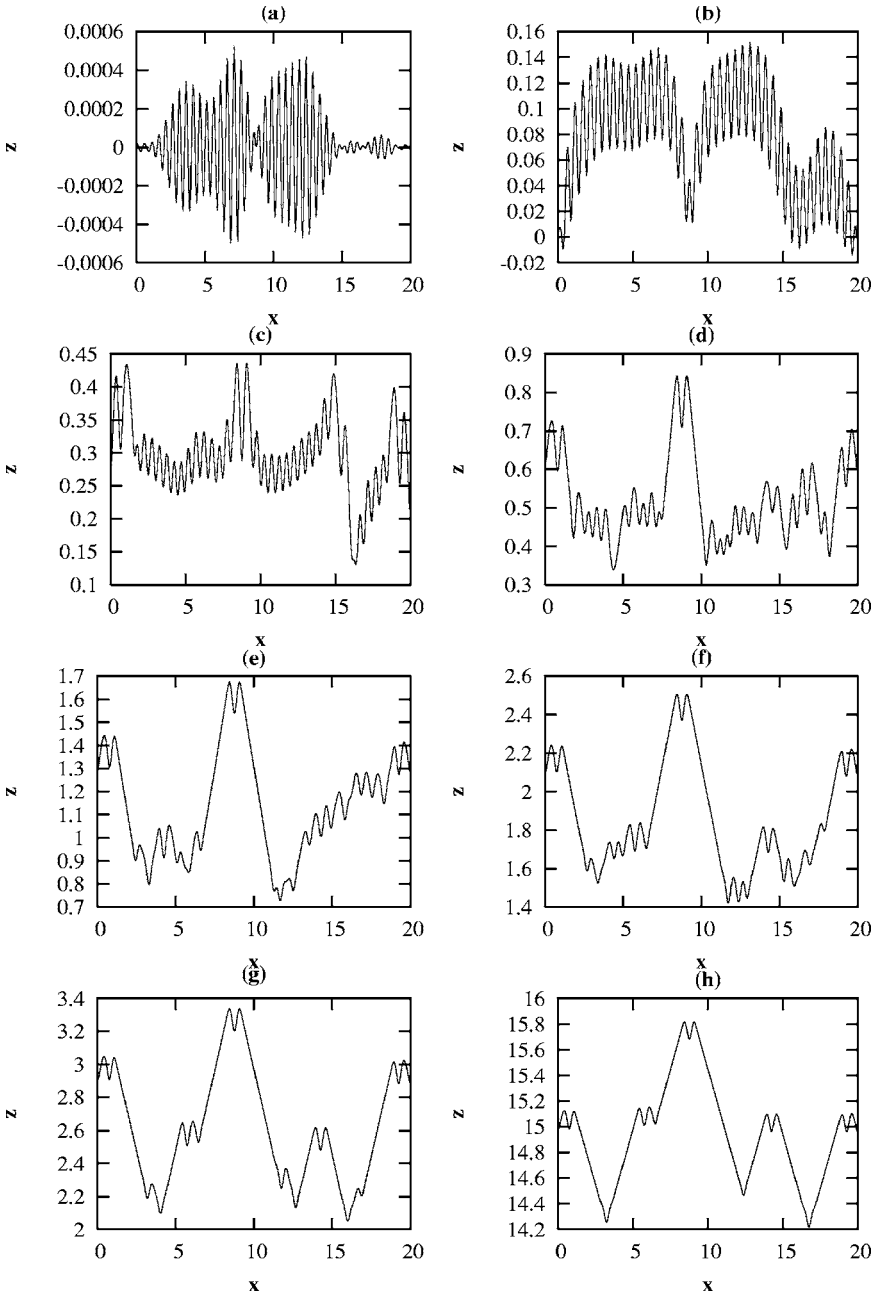

FIG. 10. Evolution of the surface shape to the stationary state for $\bar{q}=2$. $t=$(a) 5×10^7, (b) 10^8, (c) 1.5×10^8, (d) 2×10^8, (e) 3×10^8, (f) 4×10^8, (g) 5×10^8, and (h) 2×10^9.

$$h_{xx}(i+1/2)=\frac{1}{2}[h_{xx}(i)+h_{xx}(i+1)], \tag{34}$$

$$\kappa_s(i+1/2)=C_{i+1/2}\frac{\kappa_{i+1}-\kappa_i}{\delta x}, \tag{35}$$

where $h_x(i)=(h_{i+1}-h_{i-1})/(2\delta x)$, $h_{xx}(i)=(h_{i+1}+h_{i-1}-2h_i)/\delta x^2$. A unit index shift to the left results in similar expressions for $h_x(i-1/2)$ and $h_{xx}(i-1/2)$. Now, curvatures κ_i and $\kappa_{i\pm1/2}$ can be computed from Eq. (6); and $\cos 4\theta|_i=1-8h_x(i)^2/[1+h_x(i)^2]^2$. κ_i and $\cos 4\theta|_i$ also are computed at four ghost points (two at each boundary, e.g., at $i=-2,-1,N+1,N+2$) by making use of the boundary conditions.

Next, approximations to κ_s at $i\pm1/2$ are computed, including those at two ghost points (one at each boundary, e.g., at $i=-1/2$, $N+1/2$):

where

$$C_{i+1/2}=\frac{1}{2}[\{1+h_x(i)^2\}^{-1/2}+\{1+h_x(i+1)^2\}^{-1/2}]. \tag{36}$$

$C_{i-1/2}$ and $\kappa_s(i-1/2)$ are computed by shifting the index to the left by one.

Then, approximations to $\kappa_{ss}(i)$ are computed, including those at two ghost points (one at each boundary, e.g., at $i=-1,N+1$):

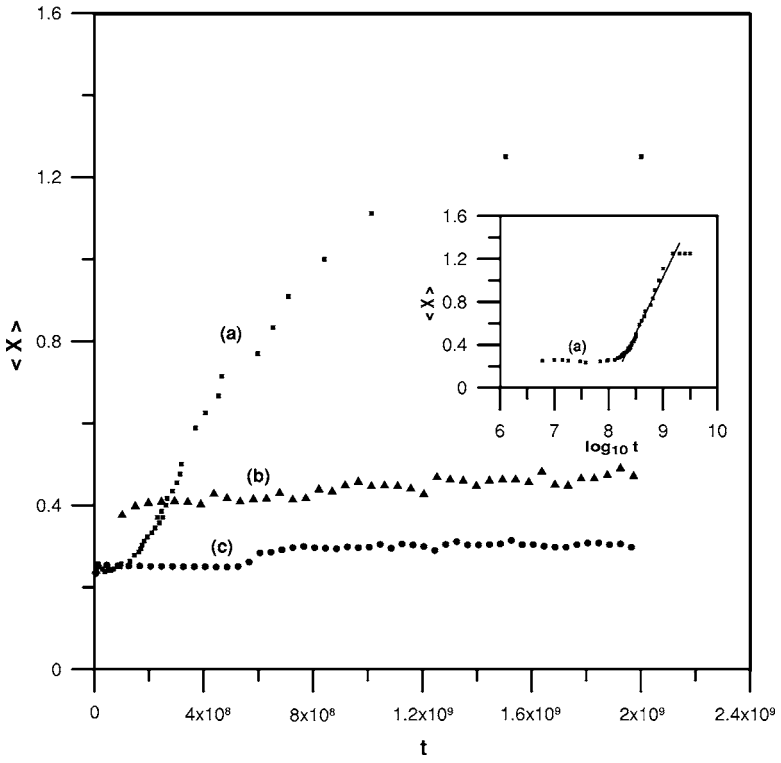

FIG. 11. Coarsening kinetics ($f=10^{-7}$). (a) $\bar{q}=2$. (b) $\bar{q}=1$. (c) Isothermal case.

$$\kappa_{ss}(i) = \frac{1}{2}[\{1 + h_x(i+1/2)^2\}^{-1/2} + \{1 + h_x(i - 1/2)^2\}^{-1/2}]\frac{\kappa_s(i+1/2) - \kappa_s(i-1/2)}{\delta x}. \quad (37)$$

Now,

$$U_i^{(+1/2)} = C_{i+1/2}\frac{\kappa_{i+1}(1 - 15\epsilon_\gamma \cos 4\theta|_{i+1}) - \kappa_i(1 - 15\epsilon_\gamma \cos 4\theta|_i)}{\delta x}, \quad (38)$$

$$V_i^{(+1/2)} = C_{i+1/2}\frac{\kappa_{ss}(i+1) - \kappa_{ss}(i) + (\kappa_{i+1}^3 - \kappa_i^3)/2}{\delta x}. \quad (39)$$

$U_i^{(-1/2)}$ and $V_i^{(-1/2)}$ are computed by shifting the index to the left by one.

To test this method, we set $f=Q_0=0$, $B=1$, $\epsilon_\gamma=0.5$, and $\Delta=0.1$ in Eq. (28) and computed the (isothermal) evolution of the small-amplitude (5×10^{-7}), random initial perturbation of the line segment $z=0$, $0\leqslant x\leqslant 2$. The result (not shown) coincides with Fig. 13 in Ref. [26]. According to Eq. (26), the spinodal wavelength in this case is $\lambda_{\max}=1$, and this is perfectly reproduced in the simulation. The growth rate dependence on time also behaves like the one computed in Ref. [26], with $\omega_{\max}=3965$ at $t=0.003$ [value predicted by Eq. (24) is 3978]. The described finite volume method is an extension of the method used in Ref. [45] for the computation of the isotropic evolution of grain boundary grooves by the surface diffusion. Also note that our discretization of the fully nonlinear KPZ term is reminiscent of the one proposed in Refs. [46,47] for the "small-slope" term $(f/2)h_x^2$. There, it was argued that finite difference schemes based on the conventional approximation of h_x do not approximate the continuum KPZ equation due to microscopic roughness.

B. Results

Evolution of the small amplitude random perturbation was computed in the interval $0\leqslant x\leqslant 20$, for values of f in $[10^{-10}, 10^{-6}]$ and $\bar{q}$ in $[0.25,8]$. The latter values are chosen so that the ratio of the domain size to λ_T is an integer. Thus periodic boundary conditions are used. We take $Q_0=0.5$, $Q_1=0.99$. The surface shapes in this section were obtained with the grid spacing $\delta x=0.02$. Each figure was recomputed with $\delta x=0.01$ and some of the large $\bar{q}$ results, with $\delta x=0.005$. Our hardware does not allow higher grid resolutions (a computation with $\delta x=0.005$ takes about 6 h on the 2.2 MHz CPU, with all optimizations). The surface shapes obtained with different resolutions are not exactly the same in some cases; the example is shown in Fig. 7. However, as this figure shows the typical features of the stationary shape are invariant with respect to performed mesh refinement. Our observations confirm this conclusion in each such case, without exceptions. For given spatial resolution, every unique stationary surface shape was confirmed by five runs with different random initial conditions.

For all numerical experiments the degree of anisotropy and regularization parameter are $\epsilon_\gamma=0.5$ and $\Delta=0.0275$. The spinodal wavelength corresponding to these values is $\lambda_{\max}=0.5$. Thus for stated values of $\bar{q}$ the ratio $0.125\leqslant\lambda_{\max}/\lambda_T\leqslant 4$. Note that even the most crude resolution ($\delta x=0.02$) samples the spinodal wavelength at 25 points. Other choices

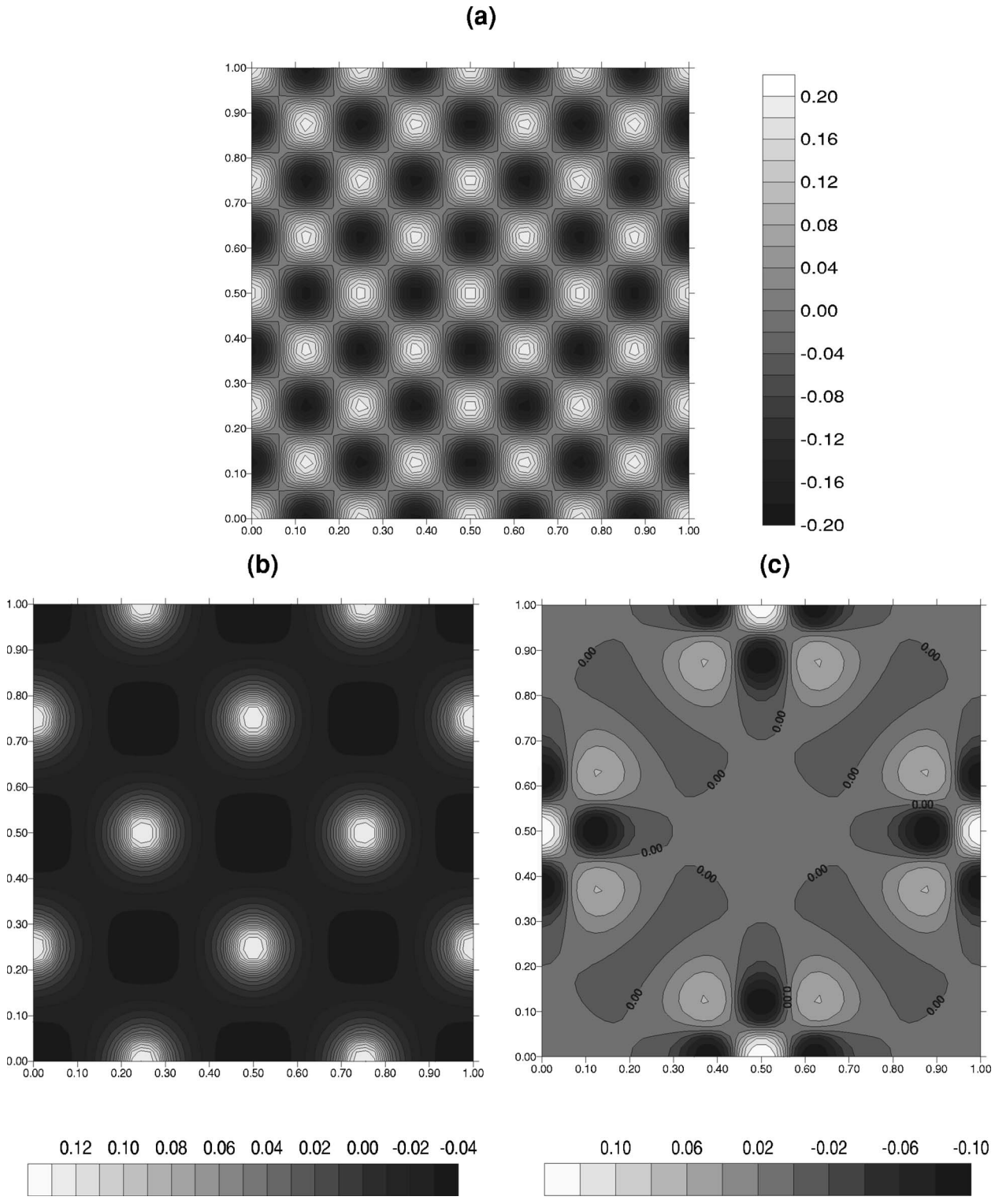

FIG. 12. Contour plots of the large-slope, 2D surface perturbation. $\epsilon_\gamma=0$, $f=10^{-9}$. (a) Plot at $t=0$. (b) (wavelength of the temperature perturbation in the x or y direction) $=2\times$ (wavelength of the surface perturbation in the x or y direction); plot at $t=5\times10^6$. (c) (wavelength of the temperature perturbation in the x or y direction) $=4\times$ (wavelength of the surface perturbation in the x or y direction); plot at $t=5\times10^6$.

for ϵ_γ and Δ exist that result in the latter ratio in the same range. For instance, choices $\epsilon_\gamma=0.5$, $\Delta=0.001\,097\,6$ and $\epsilon_\gamma=10.7899$, $\Delta=0.0275$ both give $\lambda_{\max}=0.1$, and so for, say, $\bar{q}=4$ (equivalently, $\lambda_T=0.25$) $\lambda_{\max}/\lambda_T=0.4$. However, the maximum spinodal growth rates of instability in these cases are very large [Eq. (24) predicts $\omega_{\max}=3.377\times10^7$, 8.172×10^7, respectively) making the numerical method fail. Our choice of parameters corresponds to the modest maximum

spinodal growth rate 53 798. Still, this rate is one order of magnitude higher than in Ref. [26].

Figures 8(a)–8(f) show the stationary surface shapes for $\bar{q}=0.25$, 0.5, 0.6, 0.65, 1, and 2, respectively, at time $t=2\times10^9$ and $f=10^{-7}$. Also, the stationary shape corresponding to $\bar{q}=1.5$ is shown in Fig. 7. One can notice that the stationary shape goes through a series of bifurcations as $\bar{q}$ increases. For small $\bar{q}$ values, sharply terminated hills emerge and their number equals the number of temperature perturbation wavelengths per irradiated domain [Figs. 8(a) and 8(b)]. In other words, the intrinsic spinodals coarsen in the hill-and-valley pattern with the externally induced wavelength. Quite surprisingly, and in contrast to the stable growth, hills are formed where the temperature attains its maximum value. With the increase of $\bar{q}$ the hills height and width become uniform [Fig. 8(c)]. A further increase of $\bar{q}$ results in the formation of several large domains, where each domain is composed of adjacent hills merged together [Fig. 8(d)]. For even larger values of $\bar{q}$ this structure becomes transient and subsequently coarsens into a large regular structure which spans many λ_T (and $\lambda_{\max}$) wavelengths [Fig. 8(f)]. The latter structure is composed of the hills with the straight side surfaces, but the tops of the hills are not sharp anymore; they are rough, and this roughness apparently bears the footprint of the wavelength λ_T. No trace of the faceting instability with the wavelength $\lambda_{\max}$ can be found in this final shape.

Shapes of the type shown in Fig. 8(f) persist until $\bar{q}$ is of the order 5, after which a stationary shape fails to exist. It is replaced by a surface evolving (for as long as we were able to compute) chaotically in time-space. Figure 9(a) shows a snapshot of such a surface at the same time instant, $t=2\times10^9$. Notice that the chaotic states were computed in Ref. [27], where the nonlinear, long wavelength, isothermal model is developed; they appear when too strong a deposition destroys the faceting and coarsening process induced by strong surface energy anisotropy. In Fig. 9(b) we show, for comparison, the snapshot of the isothermal surface ($Q_0=0$); this was obtained with the same f value (10^{-7}). We therefore argue that the chaotic states we observe for large values of $\bar{q}$ (small λ_T) are not numerical artifacts. Now, the conclusion is that the presence of spatially periodic surface temperature nonuniformity inhibits chaotic dynamics when the ratio $\lambda_T/\lambda_{\max}$ is not too small; for the stationary pattern to emerge, the hot and cold regions may even be contained within the spinodal wavelength, as is the case for $2<\bar{q}<5$. But when a certain threshold on a number of such regions within the spinodal wavelength is exceeded, then the faceting and coarsening process is destroyed and the chaotic evolution emerges. Similar to the model of Ref. [27], the chaotic evolution emerges also when f is above a certain threshold (e.g., the deposition is too strong). For the parameter values used here, this happens (for all values of $\bar{q}$ in [0.25, 8] when $f\sim10^{-6}$ or larger. Weak deposition can stabilize the shape even for large $\bar{q}$; for instance, stationary shapes exist for all $\bar{q}$ in [0.25, 8] when $f=10^{-9}$.

Figure 10 shows the sequence of time frames for the case $\bar{q}=2$. It could be seen that up to $t\approx2\times10^8$ the shape undergoes a rapid transition. At $t=2\times10^8$ the stationary shape is basically formed and it slowly coarsens into the final shape shown in Fig. 9(h) [and in Fig. 8(f)].

Figure 11 shows the coarsening kinetics, that is the dependence of the mean spatial scale of the coarsened structure, $\langle X\rangle$, on time. The mean spatial scale is defined as the ratio of the number of zeros of h_x in the simulation interval, to the length of the simulation interval (=20). Averaging of $\langle X\rangle$ over 12 realizations with different random initial data was performed. From Fig. 11 it could be seen that for larger λ_T the coarsening is faster and the mean scale of the structure is smaller. As the inset shows, at large times coarsening is logarithmically slow. At even larger times coarsening is extremely slow or there is no coarsening at all. These stages occur sooner for larger λ_T values, and the fastest coarsening takes place under isothermal conditions.

In conclusion of this section, the key differences between the isothermal and nonisothermal faceting in the presence of the deposition of the material on a surface are summarized as follows. First, the large structure states like those shown in Figs. 8(a)–8(g) do not emerge in the isothermal case for any value of the deposition parameter. Second, in the isothermal case the typical stationary structure is comprised of the sharply terminated hills and valleys; in the nonisothermal case the rough top hills emerge as well. Third, in the isothermal case the hills are separated by the spinodal wavelength when the deposition is absent [26] or, in the presence of (weak) deposition, by the distance which reflects the balance between KPZ-nonlinearity and the spinodal wavelength [27]. Under the nonisothermal conditions, the separation distance depends on the λ_T value rather than on $\lambda_{\max}$ and f.

ACKNOWLEDGMENTS

I am grateful to Professor Ramki Kalyanaraman for a useful discussion and for sending me the copy of Dr. Chi Zhang's Ph.D. thesis. I thank Professor Alexander A. Golovin and Professor Brian J. Spencer for reading the manuscript and providing criticisms and valuable suggestions. An anonymous referee is acknowledged for a thoughtful and timely review.

APPENDIX A: 2+1 ISOTROPIC, LARGE-SLOPE MODEL

The nondimensional evolution equation in this case reads

$$h_t = f(-1+\sqrt{1+h_x^2+h_y^2}) + B\nabla_s[(1+\alpha\langle\hat{T}^2\rangle)\nabla_s\kappa], \tag{A1}$$

where

$$\nabla_s = \vec{i}\left(\frac{(1+h_y^2)\partial/\partial x - h_x h_y\ \partial/\partial y)}{\sqrt{1+h_x^2+h_y^2}}\right) + \vec{j}\left(\frac{(1+h_x^2)\partial/\partial y - h_x h_y\ \partial/\partial x)}{\sqrt{1+h_x^2+h_y^2}}\right) \tag{A2}$$

is the surface gradient on a surface $z=h(x,y,t)$ and

$$\kappa = -\frac{(1+h_y^2)h_{xx} - 2h_x h_y h_{xy} + (1+h_x^2)h_{yy}}{(1+h_x^2+h_y^2)^{3/2}} \tag{A3}$$

is the local surface curvature. Also

$$\langle \hat{T}^2 \rangle = \frac{1}{2} Q_0^2 (1 + Q_1 \cos 2\pi \bar{q}_1 x \cos 2\pi \bar{q}_2 y)^2 \qquad \text{(A4)}$$

is the averaged square of the temperature perturbation, where $2\pi\bar{q}_1$ and $2\pi\bar{q}_2$ are the wave numbers in directions x, y.

To perform computations, first all possible differentiations in Eq. (A1) were completed. Spatial discretization of the resulting equation was done using the second order finite difference scheme with symmetry or periodic conditions at the boundaries of the square $\{0 \leqslant x, y \leqslant 1\}$. Time stepping was done using the implicit Ruinge-Kutta method.

We took the initial profile $z = 0.2 \cos 8\pi x \cos 8\pi y$ and performed computations with $f = 10^{-9}$. Figure 12 shows the contour plots of the surface at late times for cases $\bar{q}_1 = \bar{q}_2 = 2$ and $\bar{q}_1 = \bar{q}_2 = 1$. In the former case, coarsening and relaxation proceed as expected from the 1+1 case (compare to Fig. 3), but in the latter case the surface features are qualitatively different from the 1+1 case (compare to Fig. 4). One can see surface elevations near the boundaries at 0°, ±90°, and 180°, each being surrounded by three depressions; away from these features the surface is almost flat. We currently do not have an explanation of this result.

APPENDIX B: BRIEF DESCRIPTION OF THE RESULTS OF THE EXPERIMENTS BY ZHANG AND KALYANARAMAN PERTAINING TO THE MODEL PRESENTED IN THIS PAPER

The morphology that results from the interference heating consists of either (i) approximately 3-nm-height stripes of Co which are regularly spaced several hundreds of nanometers apart on the Si(100) substrate, (ii) regularly spaced lines of approximately 0.5-nm tall and 50-nm-wide nanoclusters, or (iii) irregularly shaped particles similar to rapidly solidified molten droplets. It is important to recognize that the laser fluence was insufficient to cause melting or degradation of a substrate and film (deposited energy density on a substrate is approximately 5 $\mathrm{mJ/cm^2}$ per pulse); thus surface rippling from the instabilities typically observed in high-energy laser irradiation of surfaces can be ruled out (see, for instance, Refs. [48,49] for the reviews of the latter subject). Also, the deposition and laser irradiation were started simultaneously, and therefore the assembled structures are separated on a substrate during the initial stage of growth (film is not continuous); the continuous patterned film is formed prior to termination of a growth process. For morphologies (i) and (ii), Zhang and Kalyanaraman demonstrated that the interline spacing is consistent with the theoretical two-beam fringe spacing and lies in the same direction as laser fringes. Using energy balance considerations, the temperature rise in the regions of constructive interference compared to regions of destructive interference was estimated ≈117 K. "This results in a thermal gradient of 0.3 K/nm between the peak and valley regions of 400 nm spaced fringes. Therefore, the repetitive temperature rise with each laser pulse and the associated thermal gradient is a possible driving force for the one-dimensional patterning of the Co films. The repetitive pulsing provides a repetitive anisotropic diffusion of Co within each pulse leading to an overall diffusion from the regions of higher surface temperature (regions of constructive interference) to the lower temperatures (regions of destructive interference)." [5] However, the authors did not succeed in confirming experimentally that the Co lines form in the regions of destructive interference. The morphology (iii) resulted only when the Co film is thick (the height is ≈23 nm) and the deposition rate is very high (1 nm/min). The appearance of this morphology was attributed to heating (beyond the melting threshold) of large nanoparticles through Rayleigh scattering of laser light.

[1] J. Stewart and N. Goldenfeld, Phys. Rev. A **46**, 6505 (1992).
[2] F. Liu and H. Metiu, Phys. Rev. B **48**, 5808 (1993).
[3] C. Zhang and R. Kalyanaraman, Appl. Phys. Lett. **83**, 4827 (2003).
[4] C. Zhang and R. Kalyanaraman, J. Mater. Res. **19**, 595 (2004).
[5] W. Zhang, C. Zhang, and R. Kalyanaraman, Mater. Res. Soc. Symp. Proc. **849**, 53 (2005).
[6] C. Zhang, Ph.D. thesis, Dept. of Physics, Washington University, 2004 (unpublished).
[7] O. Pierre-Louis and M. I. Haftel, Phys. Rev. Lett. **87**, 048701 (2001).
[8] X. Niu, R. Vardavas, R. E. Caflisch, and C. Ratsch, Phys. Rev. B **74**, 193403 (2006).
[9] M. Siegert and M. Plischke, Phys. Rev. Lett. **73**, 1517 (1994).
[10] J. A. Stroscio, D. T. Pierce, M. D. Stiles, A. Zangwill, and L. M. Sander, Phys. Rev. Lett. **75**, 4246 (1995).
[11] M. Rost and J. Krug, Phys. Rev. E **55**, 3952 (1997).
[12] M. Siegert, M. Plischke, and R. K. P. Zia, Phys. Rev. Lett. **78**, 3705 (1997).
[13] M. Siegert, Physica A **239**, 420 (1997).
[14] P. Politi, Phys. Rev. E **58**, 281 (1998).
[15] M. F. Gyure, J. J. Zinck, C. Ratsch, and D. D. Vvedensky, Phys. Rev. Lett. **81**, 4931 (1998).
[16] J. G. Amar, Phys. Rev. B **60**, R11317 (1999).
[17] D. Moldovan and L. Golubovic, Phys. Rev. E **61**, 6190 (2000).
[18] M. V. R. Murty, Phys. Rev. B **62**, 17004 (2000).
[19] W. W. Mullins, in *Metal Surfaces* (American Society for Metals, Metals Park, OH, 1963), p. 1766.
[20] C. Herring, Phys. Rev. **82**, 87 (1951).
[21] S. Angenent and M. E. Gurtin, Arch. Ration. Mech. Anal. **108**, 323 (1989).
[22] A. Di Carlo, M. E. Gurtin, and P. Podio-Guidugli, SIAM J. Appl. Math. **52**, 1111 (1992).
[23] A. A. Golovin, S. H. Davis, and A. A. Nepomnyashchy, Physica D **122**, 202 (1998).
[24] B. J. Spencer, Phys. Rev. E **69**, 011603 (2004).
[25] M. Siegel, M. J. Miksis, and P. W. Voorhees, J. Mech. Phys. Solids **52**, 1319 (2004).
[26] F. Hausser and A. Voigt, Interfaces Free Boundaries **7**, 353 (2005).

[27] T. V. Savina, A. A. Golovin, S. H. Davis, A. A. Nepomnyashchy, and P. W. Voorhees, Phys. Rev. E **67**, 021606 (2003).
[28] M. Burger, J. Comput. Phys. **203**, 602 (2005).
[29] F. Hausser and A. Voigt, J. Cryst. Growth **266**, 381 (2004).
[30] S. J. Watson and S. A. Norris, Phys. Rev. Lett. **96**, 176103 (2006).
[31] W. W. Mullins, J. Appl. Phys. **30**, 77 (1959).
[32] W. W. Mullins, J. Appl. Phys. **28**, 333 (1957).
[33] J. W. Cahn and J. E. Taylor, Acta Metall. Mater. **42**, 1045 (1994).
[34] H. P. Bonzel and E. Preuss, Surf. Sci. **336**, 209 (1995).
[35] A. A. Golovin, S. H. Davis, and A. A. Nepomnyashchy, Phys. Rev. E **59**, 803 (1999).
[36] J. W. Cahn, Trans. Metall. Soc. AIME **242**, 168 (1968).
[37] A. A. Golovin (private communication).
[38] M. M. Yakunkin, High Temp. **26**, 585 (1988).
[39] B. S. Yilbas and M. Kalyon, J. Phys. D **34**, 222 (2001).
[40] M. Khenner and V. K. Henner, J. Phys. D **38**, 4196 (2005).
[41] M. Khenner, Phys. Rev. E **72**, 011604 (2005).
[42] M. Kardar, G. Parisi, and Y.-C. Zhang, Phys. Rev. Lett. **56**, 889 (1986).
[43] A. Pototsky, M. Bestehorn, and U. Thiele, Physica D **199**, 138 (2004).
[44] R. P. Haskett, T. P. Witelski, and J. Sur, Physica D **209**, 117 (2005).
[45] W. Zhang and I. Gladwell, in *Numerical Treatment of Multiphase Flows in Porous Media*, edited by Z. Chen *et al.* (Springer, Berlin, 2000), p. 419.
[46] C.-H. Lam and F. G. Shin, Phys. Rev. E **57**, 6506 (1998).
[47] C.-H. Lam and F. G. Shin, Phys. Rev. E **58**, 5592 (1998).
[48] N. C. Kerr, B. A. Omar, S. E. Clark, and D. C. Emmony, J. Phys. D. **23**, 884 (1990).
[49] D. Walgraef, in *Materials Instabilities*, Proceedings of the 1st Latin American Summer School, edited by J. Martinez-Mardones *et al.* (World Scientific, Singapore, 1998).